

Cite this: *J. Mater. Chem. A*, 2021, 9, 9105

Polytritycene@CdS double shell hollow spheres with enhanced interfacial charge transfer for highly efficient photocatalytic hydrogen evolution†

Qian Liang,^{ab} Lijuan Liu,^a Zhenyu Wu,^b Haodong Nie,^b Hong Shi,^b Zhongyu Li^{*,a} and Zhenhui Kang^{†,bc}

A double-shell triptycene covalent polymer@CdS hollow sphere (TCP@CdS HS) composite has been successfully synthesized by *in situ* growing a TCP on the surface of CdS@SiO₂ spheres and then removal of the SiO₂ template *via* alkali etching. Characterization indicates that an amorphous TCP layer is coated on the thin CdS shell *via* an electrostatic self-assembly process, and the TCP layer thickness can be tuned by adjusting TCP loading. The photocatalytic hydrogen generation rate of the optimal TCP@CdS HS composite is up to 9480 μmol h⁻¹ g⁻¹ under visible-light irradiation, which is 57, 37 and 18 times higher than those of pristine CdS HS, SiO₂@CdS HS and SiO₂@CdS@SiO₂, respectively. Besides, the TCP@CdS HS composite possesses excellent stability, which is superior to that of SiO₂@CdS HS and SiO₂@CdS@SiO₂. An in-depth study of the electron transfer process and the photocatalytic mechanism was performed by *in situ* transient photovoltage experiments, which indicate that the TCP can facilitate the diffusion of hydrogen and stabilize the photoinduced electrons. This work provides an effective strategy to design novel hollow sphere heterostructures for solar energy conversion.

Received 5th February 2021

Accepted 10th March 2021

DOI: 10.1039/d1ta01081f

rsc.li/materials-a

1. Introduction

Sustainable hydrogen evolution from solar-driven photocatalytic water splitting has attracted extensive research attention due to its clean nature, high energy density, and recyclability.^{1–3} As one of the metal chalcogenides, CdS having a moderate band gap of 2.4 eV and good charge transfer characteristics has been widely studied in the field of solar energy transfer and photocatalysis.^{4–7} Nevertheless, solar-activated CdS presents low chemical stability due to severe photocorrosion as S²⁻ can be easily oxidized by h⁺ to produce S⁰.^{8–12} Photocorrosion severely restricts the application of chalcogenides and many efforts are devoted to photocorrosion inhibition, such as the construction of a yolk-shell structure,¹³ regulation of crystal sizes and morphology (CdS hollow spheres,¹⁴ quantum dots,¹⁵ and nanowires¹⁶) and formation of solid solutions. Yu *et al.* reported that N-doped graphene@CdS hollow spheres with large interfacial contact exhibited improved antiphotocorrosion

properties and photocatalytic activity.¹⁷ CdS hollow spheres (HS) with multiple light reflections and abundant active sites can be considered as a superior matrix for hydrogen generation, but still suffer from a high recombination rate and photocorrosion.^{18–20} Therefore, CdS HS as the inner shell coupled with chemically stable and porous organic polymers (POPs) as the outer layer to form a double-shell structure and suppress charge recombination are of vital importance.

Triptycene with extended π-planes is composed of three benzene units, and shows excellent electron transport ability.²¹ POPs with similar characteristics to metal-organic frameworks (MOFs) are applied in photocatalysis due to their large surface areas, good chemical stability and superior physicochemical properties.^{22–24} Triptycene-based polymers with covalent bonds are superior to MOFs with coordination bonds, generating better stability under realistic catalytic conditions.^{25,26} When triptycene-based polymers are coated onto CdS HS to form a “protective film”, it is predictable that the TCP could have a positive effect on the improvement of CdS HS stability. Besides, suitable band gaps, intimate contact area and a porous outer-surface can provide the strong driving force for the migration of the photoinduced electron-hole pairs. Taking the above mentioned advantages together, coupling CdS HS with triptycene-based polymers to construct a double-shell structure seems an intriguing method to improve hydrogen evolution. However, it is a great challenge to design and construct triptycene-based polymer@CdS HS.

^aJiangsu Key Laboratory of Advanced Catalytic Materials and Technology, School of Petrochemical Engineering, Changzhou University, Changzhou 213164, China. E-mail: zhongyuli@mail.tsinghua.edu.cn

^bInstitute of Functional Nano and Soft Materials Laboratory (FUNSOM), Jiangsu Key Laboratory for Carbon-Based Functional Materials & Devices, Soochow University, Suzhou 215123, China. E-mail: zhkang@suda.edu.cn

^cMacao Institute of Materials Science and Engineering, Macau University of Science and Technology, Taipa, 999078, Macau SAR, China

† Electronic supplementary information (ESI) available. See DOI: 10.1039/d1ta01081f

Herein, we rationally integrated a triptycene covalent polymer (TCP) and CdS HS to form a novel TCP@CdS HS composite with a double-shell geometric structure *via* an *in situ* Suzuki coupling reaction, and its photocatalytic hydrogen evolution activity was evaluated under visible-light irradiation. The effect of TCP layer thickness on photocatalytic performance was investigated. By contrast, SiO₂@CdS HS and SiO₂@CdS@SiO₂ three-layer spheres were prepared to replace the TCP as the outer layer. The optimal TCP@CdS HS composite exhibited remarkably enhanced H₂ generation compared with CdS HS, SiO₂@CdS HS and SiO₂@CdS@SiO₂. The photostability of heterostructures with two types of outer layers (TCP and SiO₂) was assessed by recycling tests. Additionally, *in situ* transient photovoltage (TPV) experiments of TCP@CdS HS were performed to verify the role of the TCP in the heterostructure and the electron transfer process. A possible mechanism for notable H₂ production over the present heterostructure is proposed and discussed in detail.

2. Experimental section

2.1 Synthesis of the SiO₂ template

Typically, 1.2 mL of NH₃·H₂O (28%) was dissolved in 10.3 mL of absolute ethanol and 4.2 mL of distilled water under vigorous stirring for 30 min. Then, 0.75 mL of tetraethoxysilane (TEOS) was added to the above-mentioned solution under continuous stirring for 4 h. White powder was obtained by centrifugation, which was then washed with distilled water and ethanol alternately several times.

2.2 Synthesis of CdS@SiO₂ spheres

4.0 mL of sodium citrate aqueous solution (1.0 M) and 1.0 mL of cadmium chloride aqueous solution (1.0 M) were added to 200 mL of aqueous suspension of SiO₂ spheres (300 mg) slowly, respectively. After stirring for 1 h, 4 mL of NH₃·H₂O (28%) and 4 mL of 1 M thiourea aqueous solution were added to the above mixture, and the suspension was heated in an oil bath at 80 °C for 3 h. After natural cooling, the yellow precipitate was centrifuged and washed with distilled water and ethanol alternately.

2.3 Synthesis of SiO₂@CdS@SiO₂ spheres

40 mg CdS@SiO₂ was added to 40 mL of ethanol and 2.0 mL of NH₃·H₂O (28%) by stirring. After that, 2.0 mL of TEOS was added rapidly by stirring for 4 h, and the obtained orange sample was filtered and washed with distilled water and ethanol.

2.4 Synthesis of SiO₂@CdS hollow spheres (SiO₂@CdS HS)

CdS@SiO₂ was added to 50 mL of 1.0 M NaOH aqueous solution and heated at 90 °C for 3 h to remove the SiO₂ template. Finally, it was dried in a vacuum drying oven to obtain CdS hollow spheres (CdS HS). 40 mg CdS HS was added to 40 mL of ethanol and 2.0 mL of NH₃·H₂O (28%) by stirring. After that, 2 mL of TEOS was added rapidly by stirring for 4 h, and the obtained

orange sample was filtered and washed with distilled water and ethanol.

2.5 Synthesis of TCP@CdS@SiO₂ spheres

TCP@CdS@SiO₂ was synthesized by a typical Suzuki reaction. A mixture of 50 mg of CdS@SiO₂, 100 mg of 2,6,14-tribromo-triptycene, 54 mg of 1,4-phenylenediboronic acid, 220 mg of K₂CO₃, 3.93 mg of triphenylphosphine and 1.44 mg of Pd(OAc)₂ were added to 15 mL of THF and 5.0 mL of distilled water under vigorous stirring for 1 h. Subsequently, the mixture was heated at 65 °C under continuous stirring for 12 h. The brown products were washed with THF and distilled water several times, and dried at 60 °C overnight under vacuum.

2.6 Synthesis of TCP@CdS hollow spheres

The as-prepared TCP@CdS@SiO₂ was slowly added to 20 mL of NaOH aqueous solution (1 M) and heated at 90 °C for 3 h to remove the SiO₂ template. Then, the brown TCP@CdS hollow spheres were centrifuged and washed with distilled water and ethanol, and finally dried at 60 °C overnight under vacuum. The as-synthesized TCP@CdS hollow spheres were termed TCP@CdS HS-*x*, where *x* represents the weight ratios of CdS to TCP (0.5, 1, 2 and 3), and the samples were denoted as TCP@CdS HS-0.5, TCP@CdS HS-1, TCP@CdS HS-2, and TCP@CdS HS-3.

3. Results and discussion

Fig. 1a displays the schematic illustration of the preparation process of TCP@CdS HS. Since the TCP with an amorphous structure has no characteristic diffraction peaks (Fig. 1b), the TCP@CdS HS composites with different TCP ratios exhibit identical peaks at 25.3°, 26.7°, 28.2°, 35.7°, 44.0°, 48.1° and 52.1°, which are indexed to the (100), (002), (101), (102), (110), (103) and (112) planes of hexagonal CdS (JCPDS no. 29-0914) (Fig. S1a†).¹⁷ As displayed in Fig. S1b,† owing to the weak crystallinity of SiO₂ nanospheres, the characteristic peaks of CdS@SiO₂, SiO₂@CdS@SiO₂ and SiO₂@CdS HS are quite similar and well matched with the hexagonal phase of CdS. The

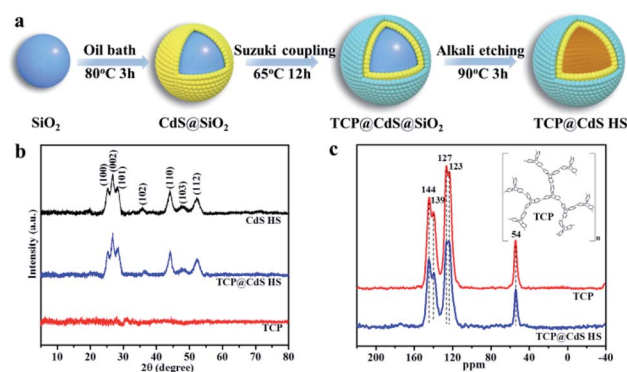


Fig. 1 (a) Schematic illustration of the preparation process of TCP@CdS HS. (b) XRD patterns of CdS HS, TCP and TCP@CdS HS-1. (c) ¹³C CP/MAS NMR spectra of the TCP and TCP@CdS HS-1.

above results demonstrate the successful formation of CdS-based photocatalysts. The solid-state ^{13}C NMR spectra of the TCP and TCP@CdS HS are displayed in Fig. 1c. Compared with the bare TCP, the TCP@CdS HS composite presents the same characteristic peaks at 54 ppm (bridging carbon atoms of the triptycene unit), 139 (144) ppm (aromatic carbon atoms of the triptycene unit) and 123 (127) ppm (aromatic carbons of boronic acid), indicating that the TCP existed in TCP@CdS HS and maintained an intact structure after the alkali etching.

The morphology of TCP@CdS HS was investigated by scanning electron microscopy (SEM) and transmission electron microscopy (TEM). The SEM image of the pristine TCP presents an irregular spherical morphology with a mean diameter of 0.6 μm (Fig. S2a \dagger), while the SiO_2 templates are homogeneous spheres with an average size of around 25 nm (Fig. 2a). For the CdS@ SiO_2 sample, it can be seen that the CdS shell coating is well-defined on the SiO_2 surface, and the outer surface of the CdS spheres is formed by small nanoparticles (Fig. 2b). Due to the strong electrostatic attraction between the TCP and CdS HS, the CdS HS can be fully wrapped by the microporous TCP *via* self-assembly, forming a hollow double-shell structure (Fig. 2c). The TEM image of CdS@ SiO_2 clearly indicates a hollow space between the CdS shell layer and the SiO_2 nanospheres (Fig. 2d), and the CdS HS seem rough and still retain the hollow structure after etching by NaOH (Fig. S2e \dagger). Additionally, the HRTEM image of the CdS HS depicts a lattice spacing of 0.334 nm, corresponding to the (002) plane of CdS (Fig. 2e). The TEM image of TCP@CdS HS confirms the formation of hollow microspheres with a double-shell structure, illustrating that the transparent TCP coating layer well wraps the CdS shell, which further demonstrates that the TCP possesses excellent stability in the etching process (Fig. 2f). Due to the amorphous structure of the TCP and the thick TCP layer grown on the thin CdS HS, the lattice fringe of the CdS HS can't be observed, and for the TCP@CdS HS-1 sample, the thickness of the CdS shell and the TCP layer is about 23 and 70 nm, respectively. It should be noted that the TCP layer thickness can be tuned by adjusting TCP loading. When the TCP loading is low (TCP@CdS HS-3), it is

difficult for the TCP layer to wrap the CdS HS and part of the CdS HS is exposed (Fig. S2g \dagger). With the increase of TCP loading, the layer thickness is increased and the thickness of TCP@CdS HS-0.5 is up to 240 nm (Fig. S2i \dagger), which can greatly affect the photocatalytic performance. As shown in Fig. S2j and k \dagger , the TEM image of SiO_2 @CdS@ SiO_2 exhibits a well-defined and uniform three-layer structure, while the hollow interior frame of SiO_2 @CdS HS is clearly observed and the thickness of the inert SiO_2 layer is approximately 30 nm. Furthermore, the elemental mapping of TCP@CdS HS ascertains that the Cd and S elements are present in the hollow spheres, and the C element is uniformly distributed in the outer layer component (Fig. 2g).

Fig. 3a shows the UV-vis DRS spectra of the TCP, CdS HS and TCP@CdS HS-1. The absorption edge of the pristine TCP is at around 435 nm due to the intrinsic π - π^* transitions of the aromatic groups, while the bare CdS HS show a strong optical absorption at 550 nm. TCP@CdS HS-1 shows improved optical absorption properties in the visible-light range, derived from the formation of the hollow sphere with a double-shell structure.²⁷ As displayed in Fig. 3b, the corresponding band gap values (E_g) of the TCP, CdS HS and TCP@CdS HS-1 are estimated to be 2.75, 2.18 and 2.13 eV, respectively. The structural porosity of the TCP, CdS HS and TCP@CdS HS was analyzed using adsorption-desorption isotherms (Fig. 3c and Table S1 \dagger). The BET surface area of the bare CdS HS is 25 $\text{m}^2 \text{g}^{-1}$, showing the typical type IV isotherm with an H3 hysteresis loop. The pure TCP presents a type I isotherm with a high surface area (1452 $\text{m}^2 \text{g}^{-1}$) and a steep N_2 gas uptake in the low pressure region, indicative of plentiful micropore structures.^{28,29} After the combination of the TCP and CdS HS, the BET surface areas of TCP@CdS HS-*x* (0.5, 1, 2 and 3) are 659, 402, 245 and 187 $\text{m}^2 \text{g}^{-1}$, respectively, showing that the specific surface area of heterostructures gradually increases with the increase of TCP loading. Furthermore, the micropore size distribution of TCP@CdS HS-0.5 is similar to that of the bare TCP with a pore size range of 0.3–0.6 nm analyzed using the HK method

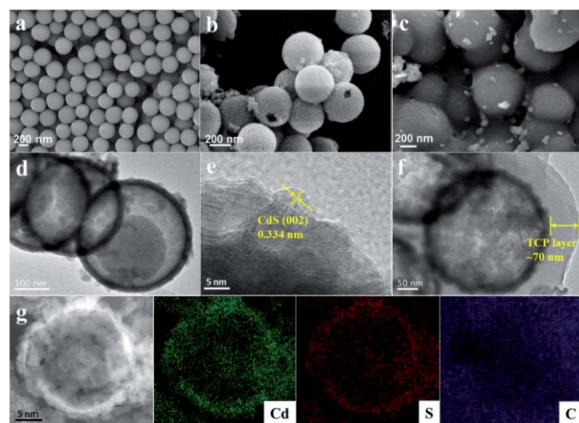


Fig. 2 SEM images of (a) SiO_2 , (b) CdS@ SiO_2 and (c) TCP@CdS HS-1. TEM image of (d) CdS@ SiO_2 , (e) HRTEM image of CdS HS and (f) TCP@CdS HS-1, and (g) EDS mapping of TCP@CdS HS-1.

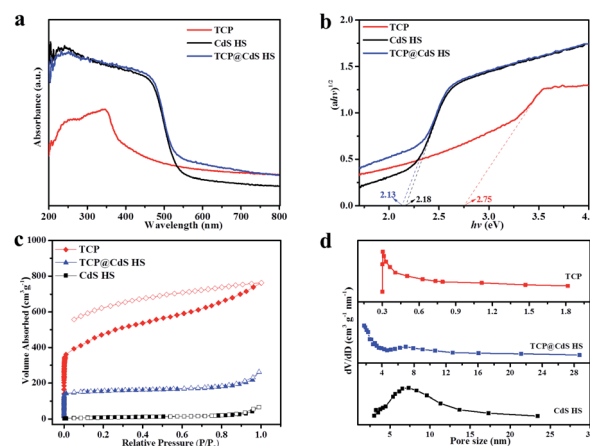


Fig. 3 (a) UV-vis DRS of the CdS HS, TCP and TCP@CdS HS-1. (b) Tauc plots of the CdS HS, TCP and TCP@CdS HS-1. (c) Nitrogen adsorption-desorption isotherms of the TCP, CdS HS and TCP@CdS HS-1. (d) Pore-size distribution of the as-prepared samples.

(Fig. S3b[†]), whereas the stacking pores observed from the CdS HS emerges for TCP@CdS HS-*x* (1, 2 and 3) with the size ranging from 5 to 15 nm calculated by the BJH method. It should be noted that TCP@CdS HS-*x* can furnish a much higher BET surface area than the bare CdS HS and many other metal chalcogenides,^{30–32} which is beneficial to provide more exposed active sites and absorb reactant molecules. The FT-IR spectra of the TCP, CdS HS and TCP@CdS HS composites are shown in Fig. S3c.[†] The absorption peak of the bare TCP at 1460 cm⁻¹ originates from the C=C bond of the aromatic ring skeleton, and several absorption peaks at 2806–3085 cm⁻¹ belong to the C-H bond. The stretching vibration at 3460 cm⁻¹ is assigned to the hydroxyl group. It is noticeable that the increasing TCP loading can strengthen the stretching vibration of the C=C bond derived from the aromatic ring. As displayed in Fig. S3d,[†] the Raman spectrum of the CdS HS presents two strong peaks at 292 and 600 cm⁻¹, assigned to the longitudinal optical mode of typical CdS, in good agreement with the previous report.³³ Similarly, the characteristic peaks of TCP@CdS HS composites emerge at 292 and 593–598 cm⁻¹, and there is no signal attributable to the TCP. Notably, the Raman peak of TCP@CdS HS at the 2LO mode exhibits an obvious red shift caused by the formed heterostructure, revealing that the TCP shell has an influence on the CdS HS.

The chemical compositions and status of the as-prepared samples were detected using XPS spectra. As shown in Fig. 4a, the representative XPS survey spectrum of the TCP@CdS HS-1 heterostructure exhibits expected C 1s, Cd 3d and S 2p. In the C 1s XPS spectra (Fig. 4b) of the pristine TCP, the peaks at 284.5 and 285.6 eV are ascribed to the C-C and C-O group, respectively.²⁵ The C 1s spectra of TCP@CdS HS are deconvoluted into three dominating peaks including two characteristic peaks of the pristine TCP and a new C-S bond at 288.7 eV, which indicates the existence of strong interaction in the heterostructure rather than a simple physical mixture.²⁶ Besides, the

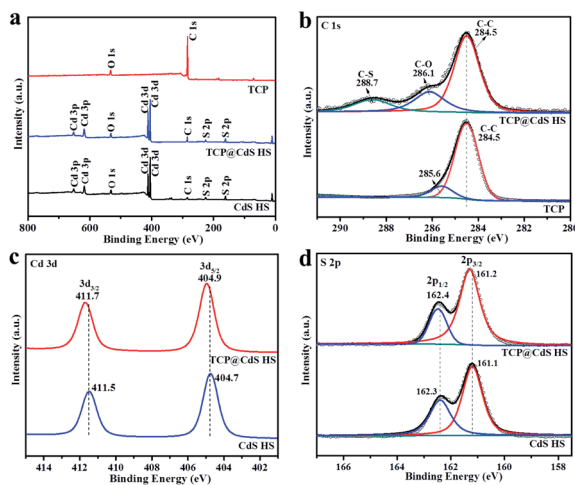


Fig. 4 (a) XPS survey spectra of the TCP, CdS HS and TCP@CdS HS-1, and high resolution XPS spectra of (b) C 1s obtained from the TCP and TCP@CdS HS-1, and (c) Cd 3d and (d) S 2p obtained from the CdS HS and TCP@CdS HS-1.

characteristic peak of the C-O bond in TCP@CdS HS is strengthened and shifted toward higher energy by ~0.5 eV, revealing the strong interaction between the TCP and CdS HS. In Fig. 4c, the binding energies of 404.7 and 411.5 eV for the CdS HS are attributed to Cd²⁺ 3d_{5/2} and Cd²⁺ 3d_{3/2}, respectively, while the corresponding Cd 3d characteristic peaks for TCP@CdS HS appear to be positively shifted to 404.9 and 411.7 eV after the formation of hollow nanospheres with a double-shell structure, suggesting that the electron transfer from the TCP to CdS HS can be achieved.³⁴ The S 2p spectrum of the CdS HS includes two peaks at 161.1 and 162.3 eV, respectively, which are allocated to S²⁻ 2p_{3/2} and S²⁻ 2p_{1/2}.³⁵ Similarly, the binding energies of TCP@CdS HS (161.2 and 162.4 eV) are higher than those of the CdS HS. As a result, the XPS results ascertain the successful formation of TCP@CdS HS heterostructures, and there is an intimate interfacial interaction and effective electron transfer between the TCP and CdS HS.³⁶

Transient photovoltage (TPV) measurements were used to further explore the process of the photocatalytic reaction over the catalysts.^{37–39} As shown in Fig. 5b, TCP@CdS HS ($t_{\max 3}$) exhibits a slower charge extraction process than the TCP and CdS HS, suggesting that the hollow sphere structure hinders the electron transmission and the electrons accumulate at the interface between the TCP and CdS HS. As depicted in Fig. 5c, attenuation constants (τ) are used to estimate the charge recombination rate of the catalysts. The attenuation constants of the TCP, CdS HS and TCP@CdS HS are 0.094 ms, 0.138 ms and 0.235 ms, respectively, indicating that the TCP@CdS HS composite presents the smallest recombination rate and the hollow sphere structure can reduce charge recombination. Furthermore, we can infer that the recombination process mostly occurs on the CdS HS because the attenuation constant of TCP@CdS HS (τ_3) is 2.5 times that of the TCP and approximately 1.7 times that of CdS. According to Fig. 5d, the area of the shadow part (A) corresponds to the maximum number of extracted electrons of the TCP, CdS HS and TCP@CdS HS,

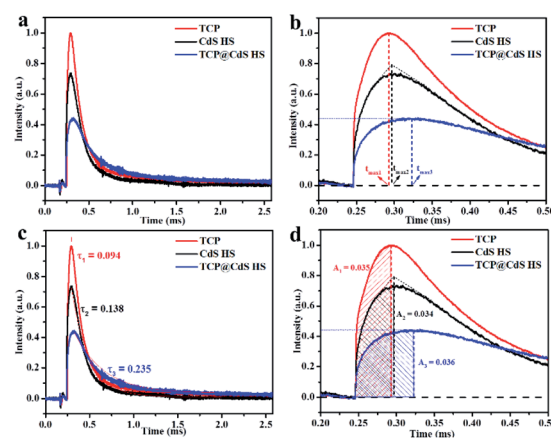


Fig. 5 (a) Comparison of the TPV of the TCP (red line), CdS HS (black line) and TCP@CdS HS (blue line). (b) Charge extraction rate (t_{\max}) of the TCP, CdS HS and TCP@CdS HS. (c) The attenuation constants (τ) of the charge recombination process. (d) The maximum electron extraction of the TCP, CdS HS and TCP@CdS HS.

which are $A_1 = 0.035$, $A_2 = 0.034$ and $A_3 = 0.036$, respectively. This result suggests that the electron extraction capability of these three samples is almost the same, as the TCP with a special hydrophobic surface structure can block the electron transmission process. Besides, the holes are verified to remain on the CdS HS, indicating that the TCP has little effect on the improvement of CdS stability, and thus a sacrificial agent should be added to consume the holes.

In order to eliminate the influence of surface properties, *in situ* transient photovoltage (TPV) measurements of the TCP, CdS HS and TCP@CdS HS were conducted under nitrogen saturated acetonitrile (Fig. 6).⁴⁰ TCP@CdS HS exhibits the highest photovoltage intensity, indicating that the special hydrophobic surface structure of the TCP indeed affects the electron transmission process. The charge extraction process is displayed in Fig. 6b, where conversely, TCP@CdS HS ($t_{\max 3}$) is the fastest compared to the TCP and CdS HS. Different from air-water-solid interfaces, nitrogen saturated acetonitrile unifies the properties of the interfaces, and TCP@CdS HS exhibits excellent capability for electron transmission. Although the recombination rate of TCP@CdS HS becomes faster ($\tau_3 = 0.125$ ms) than that of the TCP ($\tau_1 = 0.142$ ms) and CdS HS ($\tau_2 = 0.153$ ms), the maximum electron extraction of TCP@CdS ($A_3 = 0.050$) is obviously larger than that of the TCP ($A_1 = 0.008$) and CdS HS ($A_2 = 0.045$). It can be concluded that the special hydrophobic surface structure of the TCP will facilitate the diffusion of hydrogen, and therefore, the photocatalytic performance of TCP@CdS HS is predictably high.

Fig. 7a displays the H_2 production of the pristine TCP, CdS HS and TCP@CdS HS under visible-light irradiation. It can be seen that the pure TCP shows no detectable H_2 quantity owing to its weak visible-light absorption ability, while CdS HS show a relatively low H_2 production rate of $165 \mu\text{mol h}^{-1} \text{g}^{-1}$ due to their rapid charge recombination. When a TCP shell is coated on the surface of CdS HS, the amount of H_2 evolved over

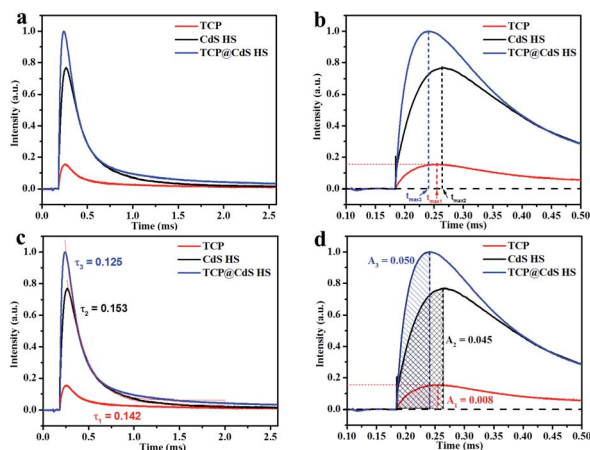


Fig. 6 (a) Comparison of the *in situ* TPV of the TCP (red line), CdS HS (black line) and TCP@CdS HS (blue line). (b) Charge extraction rate (t_{\max}) of the TCP, CdS HS and TCP@CdS HS. (c) The attenuation constants (τ) of the charge recombination process. (d) The maximum electron extraction of the TCP, CdS HS and TCP@CdS HS.

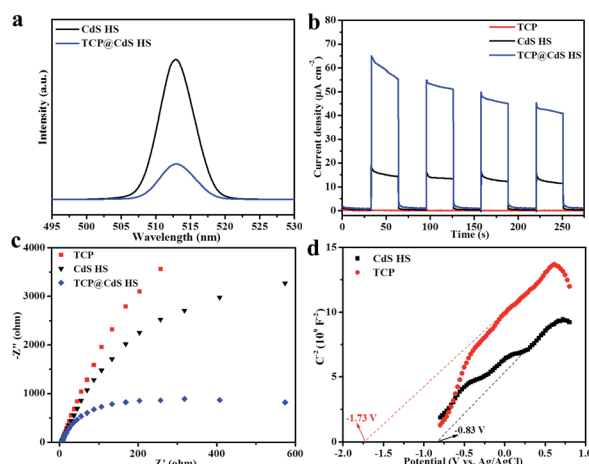


Fig. 7 (a) Photocatalytic H_2 evolution performance of the TCP, CdS HS and TCP@CdS HS-1. (b) H_2 evolution rates of SiO_2 @CdS HS, SiO_2 @CdS@ SiO_2 and TCP@CdS HS samples under visible light irradiation. (c) Recycling experiments of TCP@CdS HS-1 and CdS HS. (d) XRD patterns of TCP@CdS HS-1 before and after the reaction.

TCP@CdS HS is dramatically enhanced. The optimal TCP@CdS HS composite presents the highest H_2 production rate ($9480 \mu\text{mol h}^{-1} \text{g}^{-1}$), which is about 57 times higher than that of the pristine CdS HS. Fig. 7b presents the H_2 production rates of TCP@CdS HS composites with different weight ratios, SiO_2 @CdS HS and SiO_2 @CdS@ SiO_2 . When the TCP loading is low, it is hard to form a complete shell on the CdS HS, and part of the CdS HS is exposed to the external environment, resulting in a decreased surface area and low separation efficiency of charge carriers (TCP@CdS HS-3, $988 \mu\text{mol h}^{-1} \text{g}^{-1}$). Predictably, excessive TCP can reduce the photocatalytic H_2 evolution, caused by the formation of the shielding effect of the inactive TCP shell. Therefore, the weight ratio of the TCP represents the shell thickness and plays a key role in the photocatalytic activity of TCP@CdS HS. Furthermore, the photocatalytic H_2 production of TCP@CdS HS is compared with that of SiO_2 @CdS HS and SiO_2 @CdS@ SiO_2 with inert SiO_2 as the shell under the same conditions. The optimized photocatalytic H_2 production rate of TCP@CdS HS ($9480 \mu\text{mol h}^{-1} \text{g}^{-1}$) is 37 and 18 times higher than that of SiO_2 @CdS HS ($255 \mu\text{mol h}^{-1} \text{g}^{-1}$) and SiO_2 @CdS@ SiO_2 ($740 \mu\text{mol h}^{-1} \text{g}^{-1}$), respectively. Yao *et al.* prepared a TiO_2 -Au-CdS hollow nanoshell structure with a high H_2 production rate ($669.7 \mu\text{mol h}^{-1} \text{g}^{-1}$) under visible-light illumination.⁴¹ Bibi *et al.* reported an enhanced photocatalytic H_2 evolution ($1970 \mu\text{mol h}^{-1} \text{g}^{-1}$) over a hollow TiO_2 /CdS hybrid.⁴² As a consequence, the noble-metal-free TCP@CdS HS composite presents superior H_2 production performance, which is higher than that of many other latest reported metal chalcogenides.^{43–49}

To investigate the stabilities of CdS HS, TCP@CdS HS-1, SiO_2 @CdS HS and SiO_2 @CdS@ SiO_2 , recycling tests of H_2 production were performed under visible-light irradiation. As displayed in Fig. 7c, TCP@CdS HS-1 presents splendid stability after four cycles, whereas the H_2 evolution rate of the bare CdS HS dwindled from 165 to $100 \mu\text{mol h}^{-1} \text{g}^{-1}$, resulting from the

formation of double-shell hollow spheres and the protection effect of the TCP shell. As displayed in Fig. S4a,[†] it's interesting that the performance of SiO₂@CdS HS and SiO₂@CdS@SiO₂ reduces significantly, and especially, the H₂ production rate of SiO₂@CdS@SiO₂ decreased from 740 to 99 μmol h⁻¹ g⁻¹. The above results reveal that although the introduction of SiO₂ can improve the photocatalytic activity of CdS HS, this inert SiO₂ layer can't protect the CdS HS from photocorrosion and in contrast, it quickens the decomposition of the CdS HS. Furthermore, TCP@CdS HS-1, SiO₂@CdS HS and SiO₂@CdS@SiO₂ after photocatalytic cycling experiments were characterized by XRD and TEM. From the XRD patterns in Fig. 7d and S4b,[†] it can be observed that the characteristic peaks of TCP@CdS HS and SiO₂@CdS HS are attributed to the hexagonal phase of CdS, which is in agreement with the XRD diffraction peaks before the reaction. However, SiO₂@CdS@SiO₂ shows the diffraction peaks of both CdS and SiO₂ (broad peaks at 18°–25°), which are different from the diffraction peaks before the reaction, indicating that SiO₂@CdS@SiO₂ decomposes during the photocatalytic process (Fig. S4b[†]). TEM images of TCP@CdS HS-1, SiO₂@CdS HS and SiO₂@CdS@SiO₂ after the reaction further confirm the microstructure (Fig. S5[†]). The double-shell structure of TCP@CdS HS can be clearly observed after four consecutive cycles, revealing the good structural stability of TCP@CdS HS (Fig. S5a[†]). The TEM image of SiO₂@CdS HS after the cycling test shows that the intact CdS HS are preserved but the SiO₂ shell disappears, resulting in low photocatalytic activity and stability (Fig. S5b[†]). It is noticeable that the structure of SiO₂@CdS@SiO₂ severely collapses after the reaction (Fig. S5c[†]): only SiO₂ spheres and aggregated CdS nanoparticles are observed and the previous three-layer structure disappears, resulting in low stability.

The effective transfer and separation of photoexcited charge carriers over TCP@CdS HS are further investigated using PL spectra, transient photocurrent response and electrochemical impedance spectra (EIS). As shown in Fig. 8a, the CdS HS present the highest PL intensity, while the PL intensity of

TCP@CdS HS-1 is remarkably decreased, demonstrating that the TCP@CdS HS sample possesses a low recombination rate and effectively promotes the migration and separation of photoexcited electrons.⁵⁰ In Fig. 8b, the pristine CdS HS show limited photocurrent, while the TCP@CdS HS can remarkably improve photocurrent density, which is ascribed to the efficient separation of charge carriers. Besides, as displayed in Fig. 8c, TCP@CdS HS-1 presents a smaller arc radius than the TCP and CdS HS, suggesting the significantly improved interfacial charge transfer.⁵¹ In order to study the type of semiconductor and the band structure diagram, the flat band potentials (V_{fb}) of the TCP and CdS HS were further measured by the Mott-Schottky experiment (Fig. 8d).^{52–54} It can be seen that both the TCP and CdS HS are typical n-type semiconductors, and meanwhile, the V_{fb} values of the TCP and CdS HS are determined as -1.73 V and -0.83 V (vs. Ag/AgCl) and further equal to -1.53 V and -0.63 V (vs. NHE), respectively. Since the V_{fb} of an n-type semiconductor is approximately equal to the conduction band (E_{CB}), the band structure of a heterostructure can be evaluated based on the equation $E_{CB} = E_{VB} - E_g$. As a result, the E_{VB} values of the TCP and CdS HS are 1.22 V and 1.55 V (vs. NHE), respectively.

The proposed mechanism of H₂ generation for TCP@CdS HS is displayed in Fig. 9. From the above results of TPV, the holes mainly remain on the VB of the CdS HS, suggesting that the holes on the HOMO of the TCP are consumed by the electrons on the CB of the CdS HS. Meanwhile, the effective electron transfer from the LUMO of the TCP to the CB of the CdS HS occurs, attributable to the more negative CB of the CdS HS than the LUMO of the TCP. The residual electrons on the CdS HS can quickly reduce H⁺ to produce H₂, while the high-concentration scavenger (Na₂S/Na₂SO₃) limited to the nanoscale space of the hollow sphere can easily capture the holes on the CdS HS. Such a transfer of photoinduced charge carriers can effectively prolong the lifetime of electrons and suppress the charge recombination. Therefore, the highly efficient H₂ generation activity of TCP@CdS HS could be caused by the following reasons: (1) the TCP with a special hydrophobic surface structure can accelerate the diffusion of H₂, improve the reaction rate of the photocatalyst system, stabilize the photoinduced electrons, and enhance the separation efficiency of carriers. (2) The formed double-shell hollow structure favours intimate contact

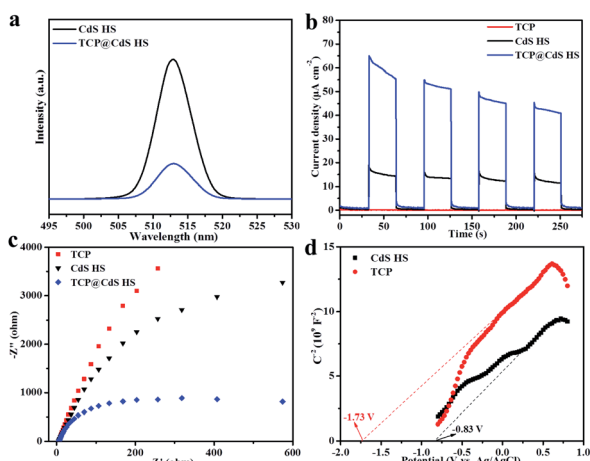


Fig. 8 (a) PL spectra, (b) transient photocurrent response, (c) EIS Nyquist plots and (d) Mott-Schottky plots of the as-prepared samples.

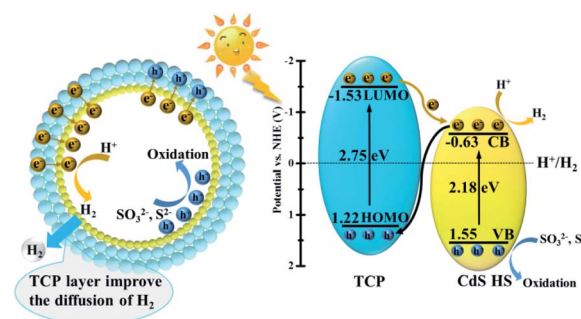


Fig. 9 Proposed charge transfer process of TCP@CdS HS under visible-light irradiation.

and a high surface to volume ratio, thus shortening the transmission distance of photogenerated electrons. (3) The hollow nanosphere can significantly improve the concentration of the sacrificial agent, which is beneficial for hole oxidation and further improves the stability of the CdS HS.

4. Conclusions

The double-shell TCP@CdS HS composites were successfully designed and constructed by an electrostatic self-assembly process. Compared with the TCP, CdS HS, SiO₂@CdS HS and SiO₂@CdS@SiO₂, the optimal TCP@CdS HS-1 with a suitable thickness (CdS shell 23 nm, TCP layer 70 nm) and a high surface area (402 m² g⁻¹) showed an enhanced H₂ production rate (9480 μmol h⁻¹ g⁻¹) under visible-light irradiation. The TPV and *in situ* TPV measurements confirm that the generated H₂ can quickly pass the hydrophobic surface of the TCP, and meanwhile the TCP can effectively stabilize the electrons accumulated at the interface. Thus, the TCP as the porous outer layer contributes to the improved performance, and the hollow sphere structure improves the concentration of Na₂S/Na₂SO₃, which can facilitate the oxidation of holes and further enhance the stability. In the present system, the “inner loop” electron transfer process over double-shell TCP@CdS HS can efficiently boost the separation and migration of charge carriers. The work demonstrates that this double-shelled hollow structure is advantageous to improve photocatalytic H₂ evolution.

5. Author contributions

Z. H. Kang and Z. Y. Li supervised the project. Q. Liang and Z. H. Kang planned the project, and Z. Y. Li designed the experiments. Q. Liang and L. J. Liu carried out materials synthesis. Z. Y. Wu and H. Shi conducted the materials characterization. H. D. Nie performed the TPV experiments. Q. Liang contributed to the manuscript writing.

Conflicts of interest

There are no conflicts to declare.

Acknowledgements

This work is supported by the National Key Basic Research Program of China (2020YFA0406104/2020YFA0406101), National MCF Energy R&D Program (2018YFE0306105), Innovative Research Group Project of the National Natural Science Foundation of China (51821002), National Natural Science Foundation of China (21703019, 21876015, 51725204, 21771132, 21471106, 51972216), Natural Science Foundation of Jiangsu Province (BK20190041), Natural Science Foundation of Jiangsu Province-Excellent Youth Foundation (BK20190102), Key-Area Research and Development Program of Guangdong Province (2019B010933001), Collaborative Innovation Center of Suzhou Nano Science & Technology, the Priority Academic Program Development of Jiangsu Higher Education Institutions (PAPD), and the 111 Project.

Notes and references

- 1 A. Kudo and Y. Miseki, *Chem. Soc. Rev.*, 2009, **38**, 253–278.
- 2 J. Liu, Y. Liu, N. Y. Liu, Y. Z. Han, X. Zhang, H. Huang, Y. Lifshitz, S. T. Lee, J. Zhong and Z. H. Kang, *Science*, 2015, **347**, 970–974.
- 3 J. X. Low, B. Z. Dai, T. Tong, C. J. Jiang and J. G. Yu, *Adv. Mater.*, 2019, **31**, 1802981.
- 4 L. Cheng, Q. J. Xiang, Y. L. Liao and H. W. Zhang, *Energy Environ. Sci.*, 2018, **11**, 1362–1391.
- 5 M. Liu, L. Z. Qiao, B. B. Dong, S. Guo, S. Yao, C. Li, Z. M. Zhang and T. B. Lu, *Appl. Catal., B*, 2020, **273**, 119066.
- 6 L. X. Zheng, F. Teng, X. Y. Ye, H. J. Zheng and X. S. Fang, *Adv. Energy Mater.*, 2020, **10**, 1902355.
- 7 B. C. Qiu, L. J. Cai, N. Zhang, X. M. Tao and Y. Chai, *Adv. Sci.*, 2020, **7**, 1903568.
- 8 B. Chica, J. Ruzicka, H. Kallas, D. W. Mulder, K. A. Brown, J. W. Peters, L. C. Seefeldt, G. Dukovic and P. W. King, *J. Am. Chem. Soc.*, 2020, **142**, 14324–14330.
- 9 X. M. Ning, Y. L. Wu, X. F. Ma, Z. Zhang, R. Q. Gao, J. Chen, D. L. Shan and X. Q. Lu, *Adv. Funct. Mater.*, 2019, **29**, 1902992.
- 10 R. Chen, Z. H. Yan, X. J. Kong, L. S. Long and L. S. Zheng, *Angew. Chem., Int. Ed.*, 2018, **130**, 17038–17042.
- 11 K. M. Cho, K. H. Kim, K. Park, C. Kim, S. Kim, A. Al-Saggaf, I. Gereige and H. T. Jung, *ACS Catal.*, 2017, **7**, 7064–7069.
- 12 Y. Shi, X. F. Lei, L. G. Xia, Q. Wu and W. F. Yao, *Chem. Eng. J.*, 2020, **393**, 124751.
- 13 Y. Su, D. Ao, H. Liu and Y. Wang, *J. Mater. Chem. A*, 2017, **5**, 8680–8689.
- 14 M. Luo, Y. Liu, J. C. Hu, H. Liu and J. L. Li, *ACS Appl. Mater. Interfaces*, 2012, **4**, 1813–1821.
- 15 F. S. Riehle and K. Yu, *Chem. Mater.*, 2020, **32**, 1430–1438.
- 16 C. Zhang, O. Cretu, D. G. Kvashnin, N. Kawamoto, M. Mitome, X. Wang, Y. Bo, P. B. Sorokin and D. Golberg, *Nano Lett.*, 2016, **16**, 6008–6013.
- 17 C. B. Bie, B. C. Zhu, F. Y. Xu, L. Y. Zhang and J. G. Yu, *Adv. Mater.*, 2019, **31**, 1902868.
- 18 Q. Zhao, B. Zhang, W. F. Yao, Q. Wu and C. P. Huang, *Catal. Sci. Technol.*, 2016, **6**, 8474–8481.
- 19 P. Zhang, S. B. Wang, B. Y. Guan and X. W. Lou, *Energy Environ. Sci.*, 2019, **12**, 164–168.
- 20 Q. M. Sun, N. Wang, J. H. Yu and J. C. Yu, *Adv. Mater.*, 2018, **30**, 1804368.
- 21 T. Ikai, T. Yoshida, K. Shinohara, T. Taniguchi, Y. Wada and T. M. Swager, *J. Am. Chem. Soc.*, 2019, **141**, 4696–4703.
- 22 Y. Byun, L. S. Xie, P. Fritz, T. Ashirov, M. Dincă and A. Coskun, *Angew. Chem., Int. Ed.*, 2020, **132**, 15278–15282.
- 23 K. W. Lin, Z. F. Wang, Z. C. Hu, P. Luo, X. Y. Yang, X. Zhang, M. Rafiq, F. Huang and Y. Cao, *J. Mater. Chem. A*, 2019, **7**, 19087–19093.
- 24 Z. C. Xiao, X. X. Huang, K. Zhao, Q. Song, R. Y. Guo, X. H. Zhang, S. K. Zhou, D. B. Kong, M. Wagner, K. Müllen and L. J. Zhi, *Small*, 2019, **15**, 1900244.
- 25 Q. Liang, G. Y. Jiang, Z. Zhao, Z. Y. Li and M. J. MacLachlan, *Catal. Sci. Technol.*, 2015, **5**, 3368–3374.

- 26 Q. Liang, S. N. Cui, S. Xu, C. Yao, M. J. MacLachlan and Z. Y. Li, *Chem. Commun.*, 2018, **54**, 3391–3394.
- 27 A. M. Elewa, M. H. Elsayed, A. EL-Mahdy, C. L. Chang, L. Y. Ting, W. C. Lin, C. Y. Lu and H. H. Chou, *Appl. Catal., B*, 2021, **285**, 119802.
- 28 S. Mondal and N. Das, *J. Mater. Chem. A*, 2015, **3**, 23577–23586.
- 29 N. Xu, S. W. Mei, Z. X. Chen, Y. J. Dong, W. J. Li and C. Zhang, *Chem. Eng. J.*, 2020, **395**, 124975.
- 30 S. Song, J. F. Qu, P. J. Han, M. J. Hülsey, G. P. Zhang, Y. Z. Wang, S. Wang, D. Y. Chen, J. M. Lu and N. Yan, *Nat. Commun.*, 2020, **11**, 4899.
- 31 H. Yoo, M. W. Lee, S. Lee, J. Lee, S. Cho, H. Lee, H. G. Cha and H. S. Kim, *ACS Catal.*, 2020, **10**, 8465–8475.
- 32 G. N. Liu, C. Kolodziej, R. Jin, S. P. Qi, Y. B. Lou, J. X. Chen, D. C. Jiang, Y. X. Zhao and C. Burda, *ACS Nano*, 2020, **14**, 5468–5479.
- 33 N. Li, Y. X. Ding, J. J. Wu, Z. J. Zhao, X. T. Li, Y. Z. Zheng, M. L. Huang and X. Tao, *ACS Appl. Mater. Interfaces*, 2019, **11**, 22297–22306.
- 34 Z. Q. Wang, Z. L. Qi, X. J. Fan, D. Leung, J. L. Long, Z. Z. Zhang, T. F. Miao, S. G. Meng, S. F. Chen and X. L. Fu, *Appl. Catal., B*, 2021, **281**, 119443.
- 35 M. Y. Zhang, Q. Y. Hu, K. W. Ma, Y. Ding and C. Li, *Nano Energy*, 2020, **73**, 104810.
- 36 X. F. Cui, J. Wang, B. Liu, S. Ling, R. Long and Y. J. Xiong, *J. Am. Chem. Soc.*, 2018, **140**, 16514–16520.
- 37 J. J. Cao, Q. Y. Wu, Y. J. Zhao, K. Q. Wei, Y. Li, X. Wang, F. Liao, H. Huang, M. W. Shao, Y. Liu and Z. H. Kang, *Appl. Catal., B*, 2020, **285**, 119817.
- 38 J. J. Cao, H. Wang, Y. J. Zhao, Y. Liu, Q. Y. Wu, H. Huang, M. W. Shao, Y. Liu and Z. H. Kang, *J. Mater. Chem. A*, 2020, **8**, 3701–3707.
- 39 Y. Sun, Y. J. Zhou, Y. Liu, Q. Y. Wu, M. M. Zhu, H. Huang, Y. Liu, M. W. Shao and Z. H. Kang, *Nano Res.*, 2020, **13**, 2683–2690.
- 40 J. Du, Y. Y. Ma, X. Xin, H. Na, Y. N. Zhao, H. Q. Tan, Z. G. Han, Y. G. Li and Z. H. Kang, *Chem. Eng. J.*, 2020, **398**, 125518.
- 41 X. X. Yao, X. L. Hu, W. J. Zhang, X. Y. Gong, X. H. Wang, S. C. Pillai, D. D. Dionysiou and D. W. Wang, *Appl. Catal., B*, 2020, **276**, 119153.
- 42 R. Bibi, H. H. Huang, M. Kalulu, Q. H. Shen, L. F. Wei, O. Oderinde, N. X. Li and J. C. Zhou, *ACS Sustainable Chem. Eng.*, 2019, **7**, 4868–4877.
- 43 D. M. Ruan, M. Fujitsuka and T. Majima, *Appl. Catal., B*, 2020, **264**, 11854.
- 44 R. K. Chava, N. Son, Y. S. Kim and M. Kang, *Inorg. Chem. Front.*, 2020, **7**, 2818–2832.
- 45 D. D. Ma, Z. Y. Wang, J. W. Shi, Y. J. Zou, Y. X. Lv, X. Ji, Z. H. Li, Y. H. Cheng and L. Z. Wang, *J. Mater. Chem. A*, 2020, **8**, 11031–11042.
- 46 J. D. Hu, C. Chen, Y. Zheng, G. P. Zhang, C. X. Guo and C. M. Li, *Small*, 2020, **16**, 2002988.
- 47 J. F. Gao, F. D. Zhang, H. Q. Xue, L. H. Zhang, Y. Peng, X. L. Li, Y. Q. Gao, N. Li and L. Ge, *Appl. Catal., B*, 2021, **281**, 119509.
- 48 L. Ma, Y. L. Chen, D. J. Yang, H. X. Li, S. J. Ding, L. Xiong, P. L. Qin and X. B. Chen, *Nanoscale*, 2020, **12**, 4383–4392.
- 49 X. J. Meng, W. L. Qi, W. D. Kuang, S. Adimi, H. C. Guo, T. J. Thomas, S. Q. Liu, Z. P. Wang and M. H. Yang, *J. Mater. Chem. A*, 2020, **8**, 15774–15781.
- 50 G. F. Liao, Y. Gong, L. Zhang, H. Y. Gao, G. J. Yang and B. Z. Fang, *Energy Environ. Sci.*, 2019, **12**, 2080–2147.
- 51 G. Wang, C. T. He, R. Huang, J. J. Mao, D. S. Wang and Y. D. Li, *J. Am. Chem. Soc.*, 2020, **142**, 19339–19345.
- 52 Z. H. Sun, Y. K. Wang, L. B. Zhang, H. Wu, Y. C. Jin, Y. H. Li, Y. C. Shi, T. X. Zhu, H. Mao, J. M. Liu, C. H. Xiao and S. J. Ding, *Adv. Funct. Mater.*, 2020, **30**, 1910482.
- 53 H. Zhong, C. Yang, L. Z. Fan, Z. H. Fu, X. Yang, X. C. Wang and R. H. Wang, *Energy Environ. Sci.*, 2019, **12**, 418–426.
- 54 Y. R. Yang, K. Ye, D. X. Cao, P. Gao, M. Qiu, L. Liu and P. P. Yang, *ACS Appl. Mater. Interfaces*, 2018, **10**, 19633–19638.